Two-layer model for photomodulated thermoreflectance of semiconductor wafers

C. Christofides,[a] F. Diakonos, A. Seas, C. Christou, M. Nestoros, and A. Mandelis[b]
Department of Natural Sciences, Faculty of Pure and Applied Sciences, University of Cyprus, P.O. Box 537, CY-1678 Nicosia, Cyprus

(Received 4 December 1995; accepted for publication 9 April 1996)

A complete theoretical analysis of the laser photomodulated thermoreflectance signal from a two-layer semiconducting wafer is presented. It is shown that the electronic and thermal properties of a thin surface layer may be determined by using the measured induced photothermal signal. Several numerical simulations are performed in order to study the influence of various electronic, optical and thermal parameters of the two-layer sample on the photomodulated thermoreflectance signal. The influence of the upper layer as well as the influence of the substrate on the signal are also discussed and parameter regimes are identified, where the characterization of the thin overlayer may be possible using this technique. © *1996 American Institute of Physics.* [S0021-8979(96)04414-3]

I. INTRODUCTION

Laser photomodulated thermoreflectance (PMTR) has been used extensively in recent years for defect diagnostics in semiconducting wafers and several theoretical models have been developed in order to improve the analysis of the results obtained by PMTR measurements.[1–3] To render the PMTR technique complete for quantitative analyses, several questions need to be answered, necessitating the development of new models suitable not only for homogeneous but also for inhomogeneous semiconductors. Special attention must be given to thin surface layers which are important for device processing in modern semiconductor technology. For example, the majority of PMTR studies have been performed on implanted semiconducting wafers which constitute a two-layer system: the substrate and the implanted surface thin film. One of the main problems in this field is that monolayer models are mostly used in order to interpret photothermally induced signals obtained from layered wafers.[1,4,5] This modeling will likely be unable to exploit small, yet significant, signal features associated with discrete or continuously varying surface layers, especially at high modulation frequencies of the pump laser beam intensity.

Wurm *et al.*[6] developed a two-layer model which can, in principle, be used for quantitative analysis of experimental data obtained from a thin implanted surface layer on crystalline silicon. Unfortunately, thermal wave effects were neglected, as well as any changes with temperature in the thermophysical properties of the optically heated semiconductor, which makes their model inadequate in the case where thermal contribution plays a dominant role, such as with amorphous implanted layers. Nevertheless, using this model, the authors calculated recombination lifetimes of amorphous implanted layers to be of the order of μs, which is too high for amorphous silicon layers.[7]

The aim of this study is the development of a rigorous two-layer model for laser PMTR which considers plasma *and* thermal effects, in order to describe the behavior of the photomodulated thermoreflectance. It is shown that this model can constitute a tool for the correct evaluation of the optical, thermal, and electronic properties of realistic situations in surface-processed wafers, especially those of the otherwise difficult to characterize surface layer.

In the next section, the mathematical development of the two-layer model is presented and some numerical simulations testing its validity are described. Section 3 presents additional numerical simulations showing the influence of the various optical, thermal, and electronic properties of the thin surface layer on the behavior of the photothermal signal. Finally, concluding remarks are presented in Sec. 4.

II. PHOTOMODULATED THERMOREFLECTANCE THEORY

The PMTR signal from a semiconductor wafer subject to photoexcitation from an intensity-modulated laser source (pump beam), and detected via a co-incident unmodulated probe beam, is the sum of thermal and plasma wave effects and can be expressed by the following relation[8]:

$$\frac{\Delta R}{R} = C_T \Delta T + C_N \Delta N, \tag{1}$$

where R is the reflectivity at temperature T, C_T and C_N are the temperature and photoexcited plasma reflectance coefficients, respectively, and ΔR, ΔT, and ΔN are the local variations in reflectivity, temperature, and plasma density, respectively. In order to evaluate ΔT and ΔN and obtain the induced photomodulated thermoreflectance signal, the complete thermal and plasma diffusion equations for an isotropic semi-infinite medium ignoring non-linear effects, must be solved[9,10]:

$$\frac{\partial(\Delta N)}{\partial t} = D_E \nabla^2(\Delta N) - \frac{\Delta N}{\tau} + \frac{\partial n_0}{\partial T}\frac{\Delta T}{\tau} + \Phi \psi_p(r) \alpha e^{-\alpha z} e^{i\omega_0 t}, \tag{2}$$

[a]Electronic mail: costasc@earth.ns.ucy.ac.cy
[b]On leave from the ''Photothermal and Optoelectronic Diagnostics Laboratory, Department of Mechanical Engineering, University of Toronto, Toronto M5S 1A4; Canada''.

$$\frac{\partial(\Delta T)}{\partial t} = D_T \nabla^2(\Delta T) + D_T \frac{E_g}{\chi}\frac{\Delta N}{\tau} + D_T\left(\frac{h\nu - E_g}{\chi}\right)\Phi\psi_p(r)\alpha e^{-\alpha z}e^{i\omega_0 t}, \tag{3}$$

where D_T and D_E are the thermal and electronic (ambipolar) diffusivities, respectively, τ is the recombination lifetime, n_0 is the equilibrium free-carrier density. Φ is the incident photon flux, ω_0 is the angular frequency ($\omega_0 = 2\pi f$; where f is the modulation frequency), χ is the thermal conductivity. E_g is the band gap energy, and $h\upsilon$ is the photon energy of the pump beam. ψ_p is the Gaussian distribution of the pump beam and is given by the expression:

$$\psi_p(r) = e^{-2r^2/a_p{}^2}, \tag{4}$$

where a_p is the laser-beam spot size. For the case of relatively low temperatures and low doping densities, the term describing intraband thermal activation (the third term on the right hand side of Eq. (2), is negligible[9–13] and will be omitted in the ensuing theoretical development. In order to solve the system of the coupled differential Eqs. (2) and (3), it is convenient to convert to their temporal Fourier-transform domain.[14] The system of the transforms can thus be written as follows:

$$\nabla^2(\tilde{\Delta}N) - \zeta_E^2(\tilde{\Delta}N) = 2\pi\frac{\Phi_{\psi_p}(r)}{D_E}\alpha e^{-\alpha z}\delta(\omega-\omega_0), \tag{5}$$

$$\nabla^2(\tilde{\Delta}T) - \zeta_T{}^2(\tilde{\Delta}\tilde{T}) = -\frac{E_g}{\chi}\frac{\tilde{\Delta}N}{\tau} + 2\pi\frac{h\nu - E_g}{\chi}\Phi\psi_p(r)\alpha e^{-\alpha z}\delta(\omega-\omega_0), \tag{6}$$

where ζ_E and ζ_T are the plasma-wave and the thermal-wave numbers, respectively

$$\zeta_E = \sqrt{\frac{1+i\omega\tau}{D_E\tau}}, \tag{7}$$

$$\zeta_T = \sqrt{\frac{i\omega}{D_T}}. \tag{8}$$

In what follows the harmonic dependence on time of both ΔN and ΔT fields will be implied throughout, and the tilde will be dropped from their Fourier transforms. Three-dimensional solutions to the diffusion equations are needed in order to evaluate the photothermal signal, Eq. (1). Considering the axial symmetry of the problem governed by the pump laser beam, a solution can be obtained by using the Hankel transformation[3] of Eqs. (5) and (6). The Hankel transform of the source term, Eq. (4), is written as follows:

$$\hat{\psi}_p(\lambda) = \int_0^\infty e^{-2r^2/a_p{}^2}J_0(\lambda r)rdr = \frac{a_p{}^2}{4}e^{-\lambda^2 a_p{}^2/8}. \tag{9}$$

The number of absorbed photons per second Φ, is given by the relation:

$$\Phi = \frac{2(1-R)P}{h\nu\pi a_p{}^2}, \tag{10}$$

TABLE I. Thermophysical, electronic, and optical parameters of the silicon substrate used in all PMTR simulations.

Material constants[a,b]	Symbols	Values
Substrate reflectivity at 632.8 nm	R	0.35
Thermal conductivity of the substrate	χ	1.5 W/cm K
Gap Energy of the substrate	E_g	1.79×10^{-19} J
Temperature coefficient of Si at 632.8 nm	C_T	1×10^{-4} K^{-1}
Plasma coefficient at 632.8 nm	C_N	1.6×10^{-22} cm^{-3}
Optical absorption coefficient of substrate	α_2	1×10^{4} cm^{-1}
Electronic diffusivity of substrate	D_{E_2}	18 cm^2/s
Thermal diffusivity of substrate	D_{T_2}	0.9 cm^2/s
Recombination lifetime of substrate	τ_2	364×10^{-6} s
Surface recombination velocity of substrate	s_2	4197 cm/s
Doping density of substrate	N_2	6×10^{14} cm^{-3}

[a]Ref. 19.
[b]Ref. 2.

where typical values for R, $h\nu$, and the incident intensity, P, are given in Table 1. Furthermore, the Hankel transformation allows the system of differential Eqs. (5) and (6) to be reduced to ordinary differential equations for the Hankel transforms $\widetilde{\Delta N}(z,\lambda)$ and $\widetilde{\Delta T}(z,\lambda)$ which are functions of the depth coordinate, z, and the spatial frequency, λ:

$$\frac{d^2\hat{\Delta}N}{dz^2} - (\zeta_E^2+\lambda^2)(\hat{\Delta}N) = 2\pi\frac{\Phi\hat{\psi}_p(\lambda)}{D_E}\alpha e^{-\alpha z}\delta(\omega-\omega_0) \tag{11}$$

and

$$\frac{d^2\hat{\Delta}T}{dz^2} - (\zeta_T{}^2+\lambda^2)(\hat{\Delta}T) = -\frac{E_g}{\chi}\frac{\hat{\Delta}N}{\tau} - 2\pi\frac{h\nu - E_g}{\chi}\Phi_{\hat{\psi}_p}(\lambda)\alpha e^{-\alpha z}\delta(\omega-\omega_0). \tag{12}$$

In the case of a two-layer, electronically active sample the above system of equations can yield a different solution for each layer in the geometry of Fig. 1, where the substrate is assumed to be semi-infinite. The various contributions to the photothermal signal are listed below. Each integration constant of the Fourier-Hankel transforms ΔN_j and ΔT_j, ($j=1,2$) is multiplied by $\delta(\omega-\omega_0)$. This factor gives the necessary selectivity of the angular frequency $\omega=\omega_0$ among all

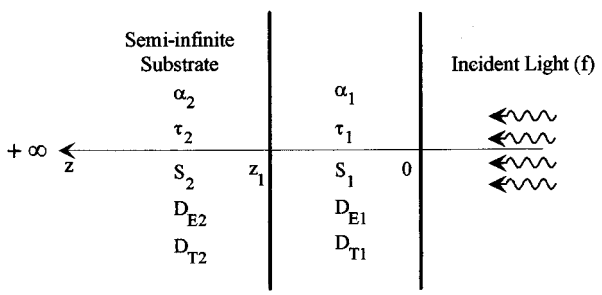

FIG. 1. Cross-sectional view of the PMTR model of an electronic material with two active layers.

possible frequencies of the resulting wideband photothermal spectrum. In what follows all factors $\delta(\omega->q_0)$ will be omitted from the calculations and all ω-dependent Fourier-Hankel transforms will be understood to yield the inverse Fourier transform automatically by setting $\omega=\omega_0$, once the inverse Hankel transform of a particular term has been calculated analytically or numerically. For the plasma contribution the solutions of Eq. (11) are:

$$\Delta\hat{N}_1(\lambda,z)=A_1(\lambda)e^{-q_1 z}+B_1(\lambda)e^{q_1 z}+C_1(\lambda)e^{-a_1 z} \qquad (0\leqslant z\leqslant z_1) \tag{13}$$

and

$$\Delta\hat{N}_2(\lambda,z)=A_2(\lambda)e^{-q_1(z-z_1)}+B_2(\lambda)e^{q_1(z-z_1)}+C_2(\lambda)e^{-\alpha_2(z-z_1)} \qquad (z_1\leqslant z<\infty). \tag{14}$$

For the thermal-wave contribution, the solutions of Eq. (12) are:

$$\Delta\hat{T}_1(\lambda,z)=Y_1(\lambda)A_1(\lambda)e^{-q_1 z}+Y_1(\lambda)B_1(\lambda)e^{q_1 z}+H_1(\lambda)e^{-p_1 z}+E_1(\lambda)e^{p_1 z}+F_1(\lambda)e^{-\alpha_1 z} \tag{15}$$

and

$$\Delta\hat{T}_2(\lambda,z)=[Y_2(\lambda)A_2(\lambda)+H_2(\lambda)]e^{-q_2(z-z_1)}+F_2(\lambda)e^{-\alpha_2(z-z_1)}, \tag{16}$$

where

$$q_1(\lambda)=\sqrt{\zeta_{E_1}^2+\lambda^2}, \tag{17}$$

$$q_2(\lambda)=\sqrt{\zeta_{E_2}^2+\lambda^2}, \tag{18}$$

$$p_1(\lambda)=\sqrt{\zeta_{T_1}^2+\lambda^2}, \tag{19}$$

and

$$p_2(\lambda)=\sqrt{\zeta_{T_2}^2+\lambda^2}. \tag{20}$$

Subscripts 1 and 2 refer to the film layer and substrate, respectively (see Fig. 1). The functions $A_1(\lambda)$, $A_2(\lambda)$, $B_1(\lambda)$, $C_1(\lambda)$, $C_2(\lambda)$, $Y_1(\lambda)$, $Y_2(\lambda)$, $H_1(\lambda)$, $H_2(\lambda)$, $E_1(\lambda)$, $F_1(\lambda)$, and $F_2(\lambda)$ in Eqs. (13)–(16) can be found by using the appropriate boundary conditions for Hankel transforms which result from the continuity and boundedress of the plasma- and temperature-waves at the various interfaces: Four boundary conditions can be written for plasma continuity and carrier flux conservation at the film substrate interface, $z=z_1$, at the surface, $z=0$, and at $z\to\infty$:

$$\left.\frac{\partial\Delta\hat{N}_1(z)}{\partial z}\right|_{z=0}=\frac{s_1}{D_{E1}}\Delta\hat{N}_1(0), \tag{21}$$

$$\Delta\hat{N}_1(z_1)=\Delta\hat{N}_2(z_1), \tag{22}$$

$$\left[D_{E1}\frac{\partial\Delta\hat{N}_1(z)}{\partial z}-D_{E2}\frac{\partial\Delta\hat{N}_2(z)}{\partial z}\right]_{z=z_1}=s_2\Delta\hat{N}_2(z_1), \tag{23}$$

$$\lim_{z\to\infty}\Delta\hat{N}_2(z)=0. \tag{24}$$

Four additional boundary conditions from the continuity of the thermal waves and heat fluxes at the various interfaces result in the following additional relationships for the Hankel transforms:

$$\left.\frac{\partial\Delta\hat{T}_1(z)}{\partial z}\right|_{z=0}=-\frac{E_{g1}s_1}{\chi 1}\Delta\hat{N}_1(0), \tag{25}$$

$$\Delta\hat{T}_1(z_1)=\Delta\hat{T}_2(z_1), \tag{26}$$

$$\left[D_{T1}\frac{\partial\Delta\hat{T}_1(z)}{\partial z}-D_{T2}\frac{\partial\Delta\hat{T}_2(z)}{\partial z}\right]_{z=z_1}=\frac{E_{g2}}{\rho_1 c_1}s_2\Delta\hat{N}_2(z_1), \tag{27}$$

$$\lim_{z\to\infty}\Delta\hat{T}_2(z)=0. \tag{28}$$

Henceforth it will be assumed that $E_{g1}=E_{g2}=E_g$. To obtain solutions, the Hankel transforms of plasma density, ΔN_j, and temperature, ΔT_j $(j=1,2)$, must be integrated over the surface of the probe beam. The two components averaged over the surface are given as a result of the convolution between the pump and probe beams[13]

$$\Delta N_1(z=0;\omega)=C_N\int_0^\infty\Delta\hat{N}_{s1}(\lambda,z=0,\omega)e^{-\lambda^2a_s^2/8}\lambda\,d\lambda \tag{29}$$

and

$$\Delta T_1(z=0;\omega)=C_T\int_0^\infty\Delta\hat{T}_{s1}(\lambda,z=0,\omega)e^{-\lambda^2a_s^2/8}\lambda\,d\lambda, \tag{30}$$

where

$$\begin{pmatrix}\Delta\hat{N}_{sj}(\lambda)\\ \Delta\hat{T}_{sj}(\lambda)\end{pmatrix}=\begin{pmatrix}\Delta\hat{N}_j(\lambda)\\ \Delta\hat{T}_j(\lambda)\end{pmatrix}e^{-\lambda^2a_p^2/8}; \quad j=1,2. \tag{31}$$

The two terms ΔN_1 and ΔT_1 are presented in the Appendix, a_s is the radius of the probe beam.

It is important to note that in the case of thin films the term $(1-R)$ in Eq. (10) is not completely correct. A more precise representation of this term should consider:[15–17] the incident power at the air-film interface, the reflection coefficient of the interface and the multiple reflections in the various layers. In the present analysis, however, multireflection phenomena and optical interference phenomena are not considered. Such effects are not significant when monochromatic light is used with wavelength outside the range of the thin-film thickness. In the case of implanted surface layers, the absence of a sharp interface between upper layer and substrate precludes the appearance of pronounced interference fringes. Furthermore (Appendix and Ref. 15), the optical interferences, and generally the presence of Φ, only influence the absolute and not the relative amplitudes of the PMTR signal.

The validity of the two-layer model was verified in the limit by comparison with existing monolayer models.[1–3,10,18] For this purpose two identical layers (same physical properties) were used in the simulation. The surface recombination velocity at the interface, $z=z_1$, was taken equal to zero. This consideration leads to the annihilation of the interface as a charge trapping region, making the two layers identical and

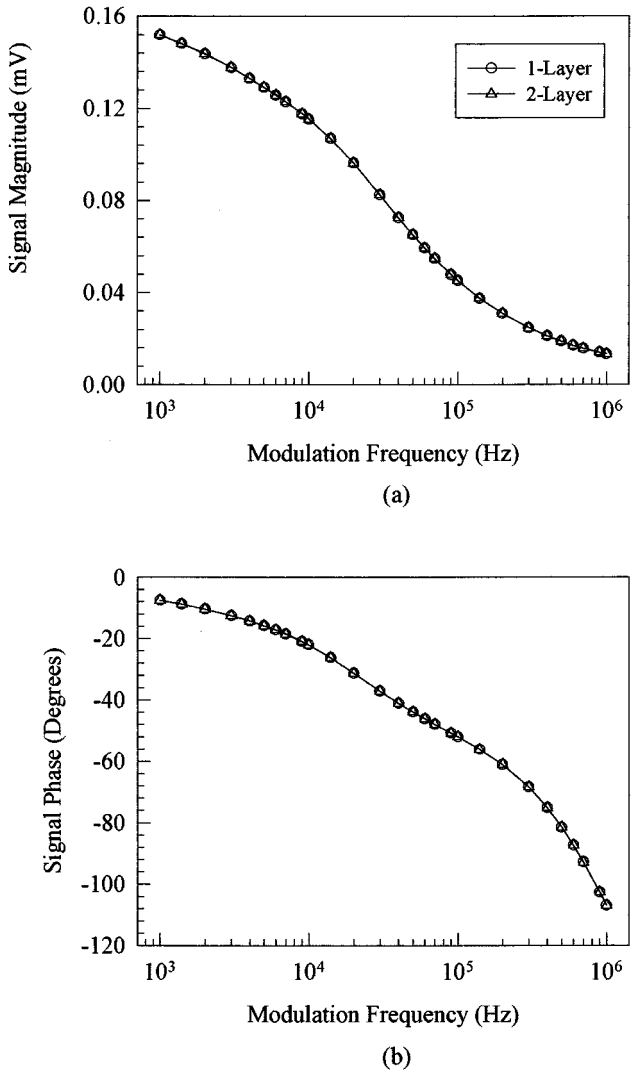

FIG. 2. PMTR signal vs frequency for Si: (△) Two-layer model and (○) monolayer model; (a) Amplitude and (b) Phase. All material constants were obtained from Tables I–III.

equivalent to a homogeneous single layer system. The numerical simulations using the two models are presented in Fig. 2 where it is clearly shown that the monolayer and two-layer models yield identical responses. The actual numerical values obtained from the simulations from the two models differ by less than 0.1% for the amplitude calculation and less than 1% for the phase calculation. The small differences are the results of round-off errors due to different computer packages (Mathcad and Fortran 77) used for the evaluation of integrals involved in the Hankel transformation.

III. PARAMETRIC INVESTIGATIONS OF THE PMTR SIGNAL

Nearly all of the previously mentioned parameters, including s_i, τ_i, D_{Ei}, D_{Ti} and α_i (with $i=1,2$) exhibit a dependence on impurity ion concentration, which affects the photothermal signal. Initially, these electronic, optical, and thermal parameters were fixed for the crystalline silicon substrate layer 2 (see Table I). By changing the surface film (layer 1) parameters (see Table II) an estimation was made of the influence of these parameters on the total PMTR signal. Based on these results, it will be seen that the present two-layer model offers the possibility of quantitative nondestructive evaluation of thin implanted layers on thick (industrial) semiconductor substrates. The values of the experimental constants used in the simulations are given in Table III.

TABLE II. Thermophysical, electronic, and optical parameters of the surface thin film used in all PMTR simulations.

Material constants[a,b]	Symbols	Values
Optical absorption coefficient of the film	α_2	5×10^4 cm^{-1}
Electric diffusivity of the film	D_{E_1}	10 cm^2/s
Thermal diffusivity of the film	D_{T_1}	0.9 cm^2/s
Recombination lifetime of the film	τ_1	5.5×10^{-6} s
Surface recombination velocity of the film	s_1	2.7×10^5 cm/s
Doping density of the film	N_1	5×10^{17} cm^{-3}

[a]Ref. 19.
[b]Ref. 20.

A. Dependence on the optical properties of the overlayer

In order to study the influence of the optical absorption coefficient of the surface layer on the photomodulated thermoreflectance signal, several numerical simulations were performed by varying α_1 between 10° and 10^7 cm^{-1}. Figure 3 shows the variation of the resulting photothermal signal as a function of the modulation frequency with various optical absorption coefficients of the thin overlayer as parameters. It appears from Fig. 3(a) that the optical absorption coefficient of the thin layer has little effect on the PMTR signal amplitude. On the other hand, the phase lag [see Fig. 3(b)] can offer higher resolution in regard to the optical absorption coefficient of the thin layer at high frequencies, when the thermal diffusion depth of the photogenerated thermal wave is commensurate with the optical absorption depth and of the same order of magnitude ($\approx \mu$m) as the surface layer thickness. The phase curve is saturated at low modulation frequencies, f, where the overlayer is totally thermally thin, as expected.[21] At high f, the phase lag decreases with increasing α_1, since the thermal-wave ''center-of-mass'' (heat centroid) shifts toward the surface of the overlayer (the location of minimum thermal lag). Figure 3(b) further indicates that a high-frequency scan in a PMTR experiment may yield the value of thermal diffusivity of a semiconducting overlayer, if an independent optical measurement of its absorption coefficient can be made. Knowledge of surface layer thermophysi-

TABLE III. Experimental constant parameters.

Experimental constants	Symbols	Values
Modulation frequency	f	1–1000 kHz
Pump beam intensity	P	43 mW
Pump beam energy	$h\nu$	2.548 eV
Pump beam radius	a_p	21 μm
Probe beam radius	a_s	21 μm
Pump beam wavelength	λ_0	632.8 nm

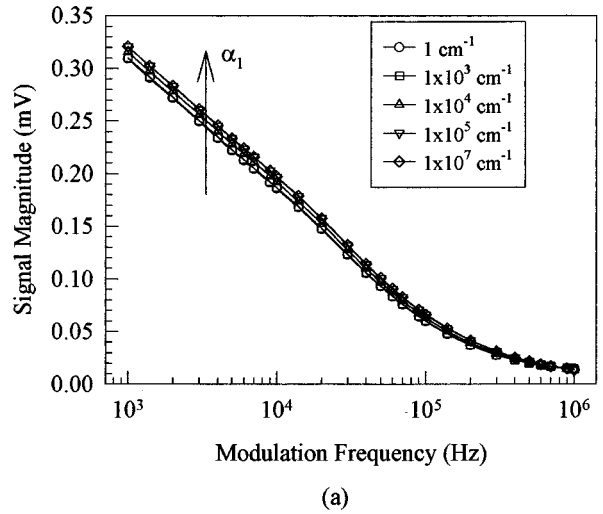

FIG. 3. PMTR signal vs frequency for various optical absorption coefficients of the thin overlayer of 1 μm thickness; (a) Amplitude and (b) Phase. All other constants of the two layers are given in Tables I–III.

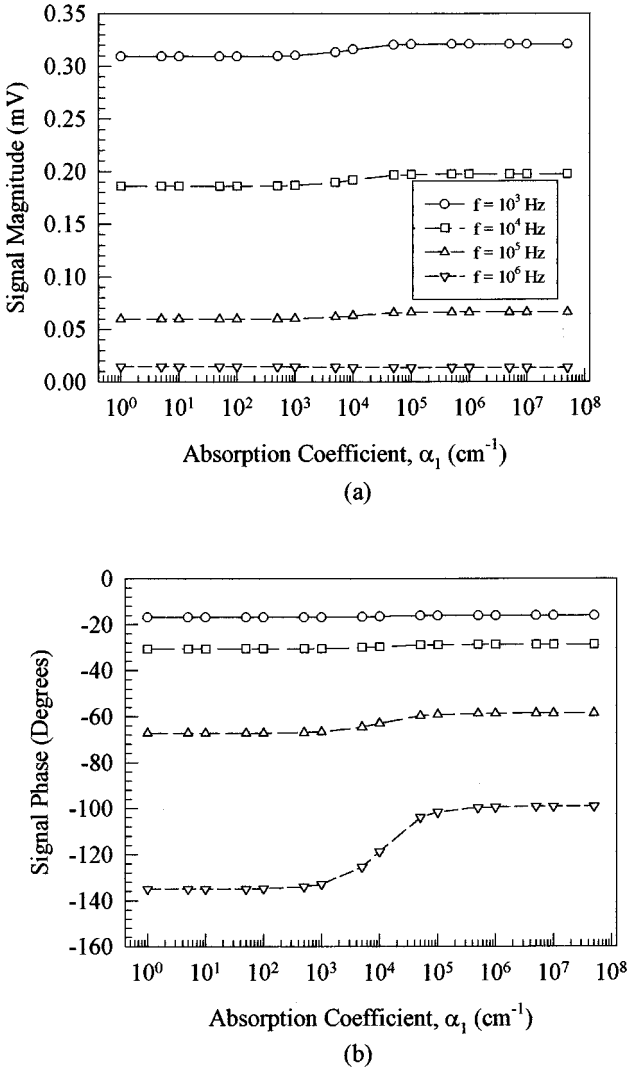

FIG. 4. PMTR signal vs overlayer optical absorption coefficient, α_1, for various modulation frequencies; (a) Amplitude and (b) Phase. All other constants of the two layers are given in Tables I–III.

cal properties is otherwise difficult to obtain and of major interest owing to their control of the thermal stability and electronic performance of processed devices.

Figures 4(a) and 4(b) present the variation of the photothermal amplitude and phase, respectively, as a function of the optical absorption coefficient α_1 of the film, with different modulation frequencies as parameters. Consistently with Fig. 3, the signal amplitude is not highly dependent on the absorption coefficient of the overlayer. The phase is more sensitive to α_1 especially at increased frequencies. At 1 MHz three regimes are evident: For $\alpha_2 < 10^3$ cm^{-1} the film is optically thin, whereas for $\alpha_2 > 10^5$ cm^{-1} the film is optically opaque.

The phase lag decreases with increasing α_1 as discussed in Fig. 3, with the transition region occurring when the optical absorption depth α_1^{-1} becomes commensurate with the thermal diffusion length in the bilayer structure. Photothermal saturation sets in at $\alpha_1 > 10^6$ cm^{-1}, when the optical absorption depth of the overlayer (and of the entire structure) becomes much shorter than the thermal diffusion length ($\approx$5.5 μm). For frequencies less than 10 kHz, the film is entirely thermally thin and therefore no variation in the signal phase is observed, whereas the PMTR signal amplitude increases slightly linearly between 10^3 and 10^4 cm^{-1}.

B. Dependence on the electronic properties of the overlayer

Figure 5 presents the signal amplitude as a function of the modulation frequency with various electronic diffusion coefficients D_{E_1} of the thin overlayer as parameters between 10^{-4} and 18 cm^2/s. For amplitude signals, Fig. 5(a), D_{E_1} plays a significant role, especially for modulation frequencies less than 10^5 Hz. The ''bend'' around $f = 10$ kHz exhibited by all curves in Fig. 5 is due to the stored energy in the electronic (plasma) system of the overlayer above the frequency where $\omega_0 \tau_1 \approx 1$ occurs. The signals shown are dominated by the thermal component of PMTR due to the optical heating of the lattice. At low frequencies the non-monotonic behavior of the curves with increasing D_{E_1} is the result of

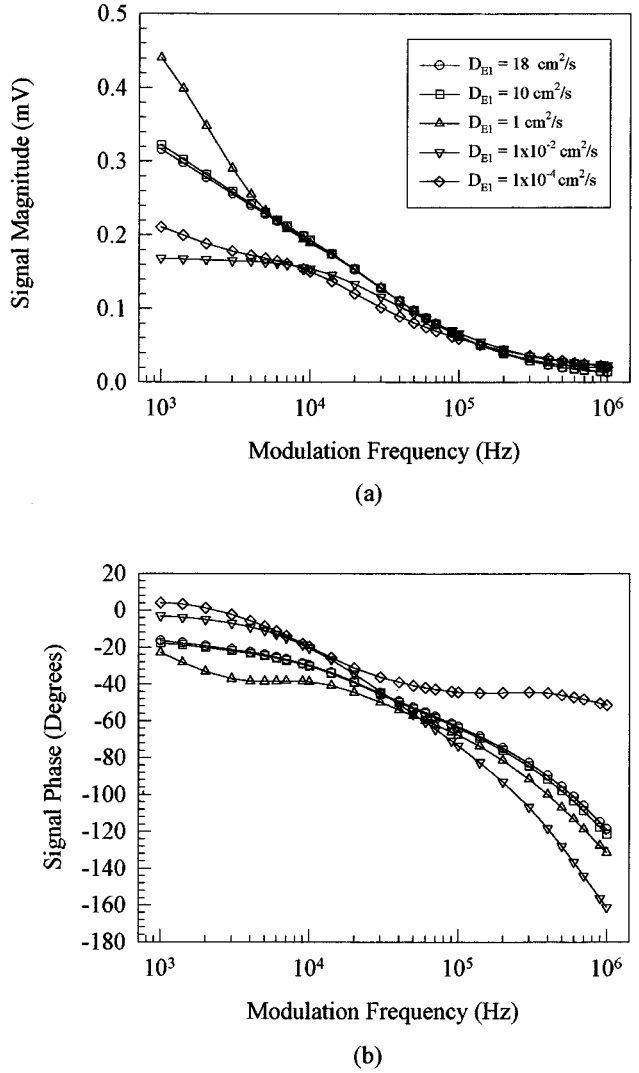

FIG. 5. PMTR signal vs frequency for various electronic ampibolar diffusivities D_{E_1} of the thin layer; (a) Amplitude and (b) Phase. All other constants of the two layers are given in Tables I–III.

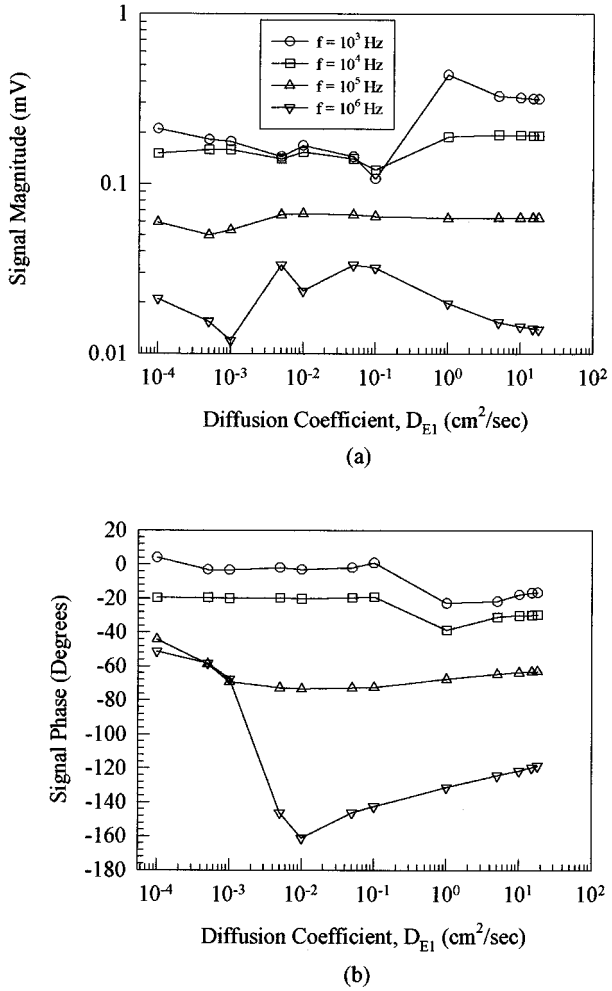

FIG. 6. PMTR signal vs ambipolar diffusion coefficient D_{E_1} of the thin overlayer, for various modulation frequencies; (a) Amplitude and (b) Phase. All other constants of the two layers are given in Tables I–III.

several competing processes: At very low D_{E_1}, curve $\diamond$, the photoexcited plasma releases its stored energy locally as a component of the measured thermal-wave fraction of the overall signal; as D_{E_1} increases a portion of photogenerated free carriers diffuse outside the area of the probe beam, which depresses the overall signal (curve $\triangledown$). A further increase in D_{E_1} (curve $\triangle$) enhances significantly the free plasma density component of the PMTR signal, which, in turn, generates an enhanced thermal-wave contribution at low frequencies, through nonradiative energy conversion. Further increases in D_{E_1}, although capable of generating increased free-carrier densities, result in lower PMTR amplitudes (curves $\square$, $\bigcirc$), because the diffusive carrier losses out of the probed region of the overlayer also increase and saturate for $D_{E_1} \geqslant 18$ cm^2/s. Overall, the deconvolution of the various plasma- and thermal-wave contributions to the PMTR signal as a function of the carrier diffusion coefficient of the overlayer is complicated, yet the effect of this layer in shaping the frequency response of the entire two-layer structure is significant. The phase responses at low frequencies, Fig. 5(b), follow similar trends to those of the amplitudes, with the more positive phases indicating a higher weight of the thermal-wave component. At high frequencies, in particular, the wide separation of the phase curves offers additional and valuable information on the relative strengths of the two signal components which, when taken independently, differ by 180° owing to the opposite signs of C_T and C_P, Eq. (1). On the other hand, the PMTR amplitudes essentially saturate at high frequencies, Fig. 5(a), such that $\omega_0 \tau_D > 1$: They become dominated by roughly equal contributions between the lattice-generated thermal-wave and the plasma-wave and independent of the free-carrier diffusion coefficient of the overlayer. Here τ_D is the carrier diffusion time out of the probe beam-defined area of radius a_s: $\tau_D \approx a_s^2/D_{E_1}$.

Figure 6 presents the variation of the PMTR signal as a function of the electronic ambipolar diffusion coefficient D_{E_1} of the film, with different modulation frequencies as parameters. Further insights on the role of this important parameter may be obtained from this type of plot. The general trend in the amplitude signal, Fig. 6(a), is the well-

known monotonic decrease with increased modulation frequency. The non-monotonic features along each curve can be explained (i) by the increased free-carrier densities with increasing D_{E_1}, contributing to the overall thermal-wave dominated PMTR signal through nonradiative recombination, followed (ii) by the decreased locally probed densities as they diffuse away from the interrogated region faster, when D_{E_1} becomes very large. The phase curves exhibit increased lags with increasing frequency, gradually shifting toward a plasma-wave domination manifested by the large phase change in the negative direction, Fig. 6(b). Nonradiative recombination contributions to the thermal-wave component decrease with increasing D_{E_1} at high f, such that $\omega_0\tau_1>1$, with either larger free-carrier densities storing the optical energy or simply moving out of the probed region at very high D_{E_1}'s carrying along the photoexcitation energy. Consistently with earlier remarks, the PMTR phase offers a much higher resolution of small dominating signal differences than the amplitude, e.g. by the plasma component at high f, between otherwise roughly equal components of opposite sign (see Fig. 6(a), ∇)

Figure 7 presents the PMTR signal amplitude and phase as a function of the modulation frequency for various recombination lifetimes τ_1 for the thin-film layer, between 10^{-9} and 10^{-4} sec. In all cases, the recombination lifetime, τ_2, of the substrate was assumed to be 364 μs.[19,20] The recombination lifetime of the surface layer plays an important role on the PMTR signal amplitude: At very low τ_1, nonradiative recombination produces a large, dominating thermal-wave component of the total signal, Fig. 7(a), curve ○. As τ_1 increases, the free-carrier plasma wave component rises significantly and monotonically, thus depressing the amplitude of the total signal owing to the negative sign of the plasma reflection coefficient C_N, Eq. (1). The PMTR phase also shifts to negative values with higher τ_1, as a result of the increased strength of the free-carrier component. At very high $\tau_1(>10^{-6}$ sec) the plasma-wave component saturates, thus forcing the PMTR amplitude and phase themselves to saturate. The signal amplitude cross-overs observed in Fig. 7(a) at $\sim 10^4$ Hz are due to the fact that at low frequencies, an increase in τ_1 retains the absorbed optical energy stored for an increased time before releasing it as heat, which subsequently diffuses away from the probed volume, mostly into the substrate. Therefore, it turns out that for $\tau_1>10^{-8}$s a relatively small, but measurable, increase in the thermal-wave component occurs at low f as more of the relatively later appearing, nonradiatively released, energy is probed before its out-diffusion as compared to thermal energy deposited earlier, which, therefore, had more time to diffuse out of the probed region. These small energy increases are clearly limited by the recombination lifetime. This effect saturates for $\tau_1>10^{-5}$ s. At high frequencies the relatively stronger increase in the plasma component with τ_1 dominates any thermal gains due to constrained out-diffusion. The result is the observed signal amplitude crossover. The trends shown in Fig. 7 can be experimentally important, because they can be accosted in cases where one performs measurements, e.g. on amorphous silicon deposited on a crystalline substrate

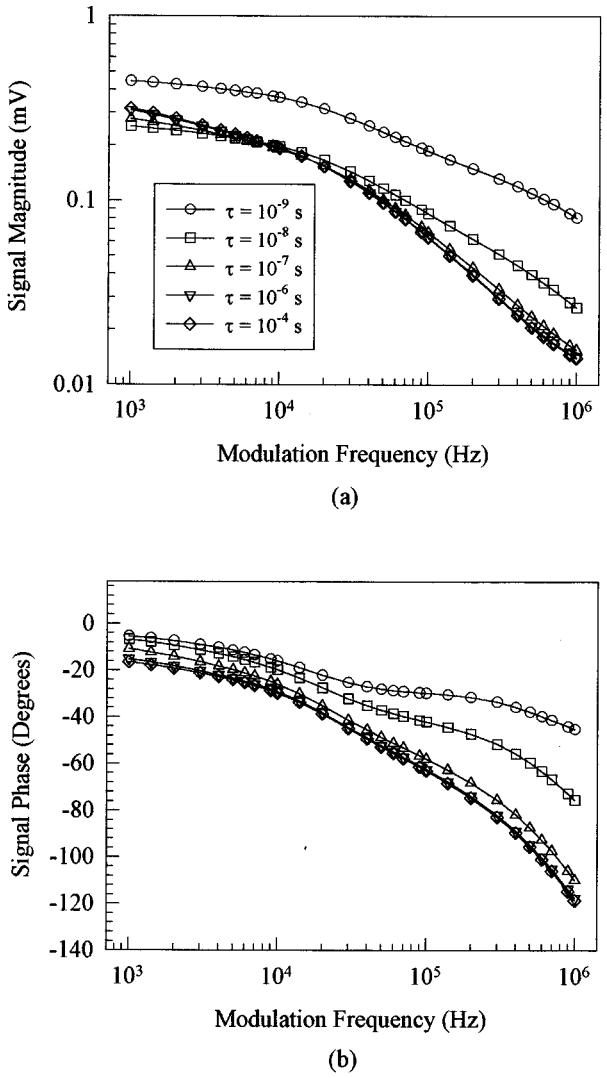

FIG. 7. PMTR signal vs frequency for various lifetimes τ_1 of the thin overlayer; (a) Amplitude and (b) Phase. All other constants of the two layers are given in Tables I–III.

with deposition process-dependent lifetime. A different viewpoint of the same phenomena can be obtained, by studying Fig. 8 which presents PMTR amplitude and phase vs recombination lifetime with the modulation frequency as a parameter. For all frequencies the PMTR amplitude generally decreases monotonically with increasing lifetime as expected from the enhanced plasma-wave component as discussed in the context of Fig. 7. This behavior was observed experimentally on a-Si films with very fast lifetimes.[22] The non-monotonic behavior of the low-frequency curve ○, Fig. 8(a), is due to the increased efficiency of heat transfer mechanism (thermal-wave) by free carriers in the overlayer with suitably delayed nonradiative recombination. This effect corresponds to the mechanism causing the amplitude cross-overs in Fig. 7(a).

The surface recombination velocity, s, is a phenomenological parameter that expresses the probability of recombination at the surface of the sample and its effects are somewhat similar to the recombination lifetime in thin-film layers, where ''surface'' and ''bulk'' are not clearly separate re-

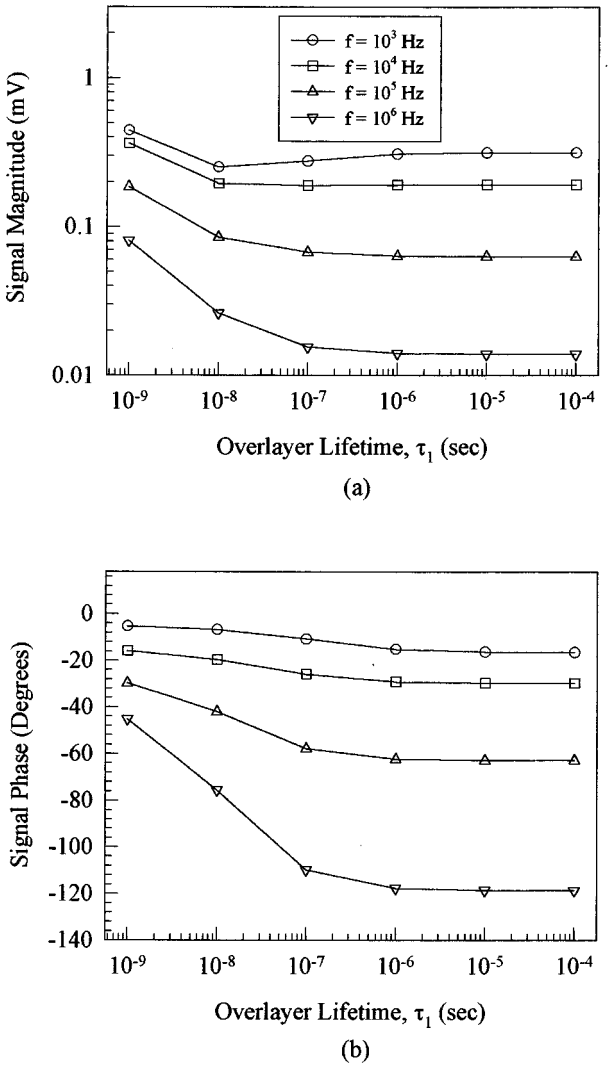

FIG. 8. PMTR signal vs lifetime τ_1 of the thin overlayer, for various modulation frequencies; (a) Amplitude and (b) Phase. All other constants of the two layers are given in Tables I–III.

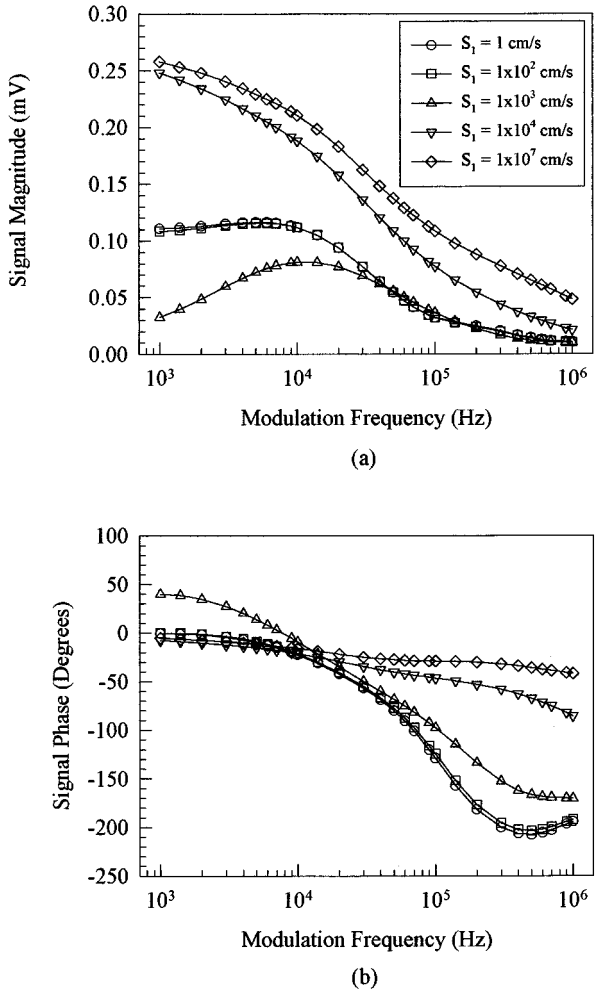

FIG. 9. PMTR signal vs frequency for various surface recombination velocities s_1 of the thin overlayer; (a) Amplitude and (b) Phase. All other constants of the two layers are given in Tables I–III.

gions. The main difference between s and τ is the fact that τ is inversely proportional to the recombination probability.[20,23] Low recombination probability is expressed with high values for τ_1 and small values for s_1. Considering this fact, the free-carrier concentration dependence of s_1 was taken to be the inverse of that of τ_1. Figure 9 presents the variation of the PMTR signal vs modulation frequency for various surface recombination velocities s_1, of the overlayer. In all cases, the interface recombination velocity, s_2, was assumed to be 4197 cm/s.[19] Interesting observations corresponding to the lifetime dependencies can be made here. The general trend in Fig. 9(a) is an increase of the PMTR signal with increasing $s_1 > 10^3$ cm/s. This is due to the suppression of the plasma-wave component and efficient conversion of the optical energy to heat on the overlayer surface, resulting from high values of s_1. For $s_1 < 10^4$ cm/s, a strong plasma-wave component forces the phase, Fig. 9(b), to take on very negative values at high frequencies, a sign of its domination by the plasma-wave. The slight amplitude inversion at low frequencies for curves ○, □ in Fig. 9(a) is due to a small decrease in thermal-wave component with $s_1 = 1 \times 10^2$ cm/s because of enhanced heat out-diffusion from the probed sample volume. The same mechanism is also responsible for the appearance of the very mild PMTR amplitude peak at $f \approx 10^4$ Hz, in curves, □ and ○ and of the well-resolved peak for curve △. The simulations have shown that this peak shifts slightly to higher frequencies for $s_1 > 10^2$ cm/s and becomes most pronounced in the range $s_1 \approx 10^3$ cm/s, curve △, where the thermal-wave sampling rates (modulation frequency) becomes commensurate with the surface and interface heat release rate due to the similar values of surface (s_1) and interface s_2 recombination velocities. This ''matching-rate'' condition minimizes the out-of-probed-volume heat-diffusion losses and becomes responsible for the emergence of PMTR signal peaks, whose frequency position may thus be used to estimate s_2, a very difficult parameter to measure with other techniques.

The s_1 dependence of the PMTR signal with modulation frequency as a parameter is shown in Fig. 10. The high-s_1 regions in the amplitude channel saturate at levels higher than the low-s_1 regions, as expected, due to the enhanced optical-to-thermal energy conversion in the former regions.

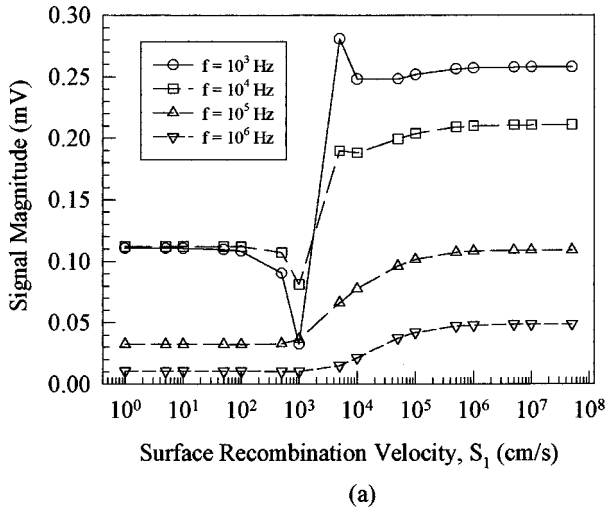

(a)

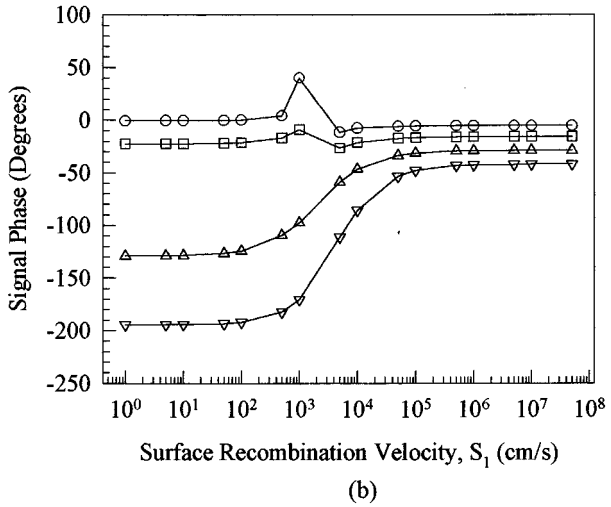

(b)

FIG. 10. PMTR signal vs surface recombination velocity s_1 of the thin layer, for various modulation frequencies; (a) Amplitude and (b) Phase. All other constants of the two layers are given in Tables I–III.

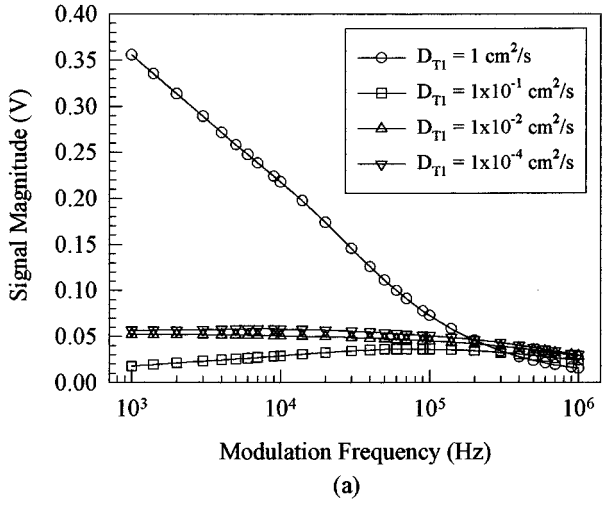

(a)

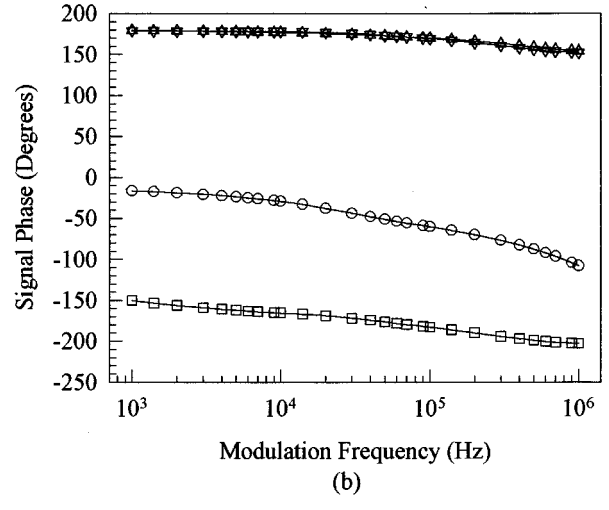

(b)

FIG. 11. PMTR signal vs frequency for various thermal diffusivities D_T of the thin layer; (a) Amplitude and (b) Phase. All other constants of the two layers are given in Tables I–III.

Consistently the phases are dominated by thermal-wave effects in the high-s_1 regions, irregardless of the frequency. In the low-s_1 regions, the high-frequency phases ($f \geq 10^5$ Hz) are mainly due to plasma-wave contributions and thus undergo very strong shifts toward less negative values across the transition region (10^3 cm/s$<s_1<10^5$ cm/s). The low-frequency phases preserve the thermal-wave dominance almost throughout the entire s_1 range, with the exception of the transition region. The ''matching-rate'' condition discussed in the context of Fig. 9, which yields a PMTR signal peak (most pronounced for $s \approx 10^3$ cm/s) is responsible for the anomalies exhibited in the transition region of Fig. 10, namely the undershoot/overshoot extrema in Fig. 10(a), curves ○,□ and similar features in the respective curves of Fig. 10(b). Experimentally, the matching-rate condition may be used in a plot like Fig. 10 to extract the difficult-to-measure interface recombination velocity s_2 from low frequency PMTR signals, provided samples are available with controlled but variable overlayer recombination velocity, s_1.

C. Dependence on the thermal properties of the overlayer

Figure 11 presents the variation of the PMTR signal as a function of the modulation frequency with various thermal diffusivities D_{T_1} as parameters in the range of 1 to 1×10^{-4} cm^2/s. It can be seen that the signal amplitude depends strongly on D_{T_1} especially at low modulation frequencies. As expected, at high modulation frequencies it is very difficult to measure the influence of D_{T_1} on the photothermal amplitude since this regime is dominated by the plasma component. Figure 11(b) shows that the phase signal is much more sensitive to the influence of the thermal properties of the overlayer. The various non-monotonic trends in Fig. 11 are easier to understand with the help of the plots in Fig. 12. This figure shows the dependence of the PMTR signal on thermal diffusivity D_{T_1} at constant frequency, with various frequencies as parameters. The constant signal levels (amplitude, Fig. 12(a), and phase, Fig. 12(b)) at very low diffusivities are indicative of semi-infinite solids, in which the

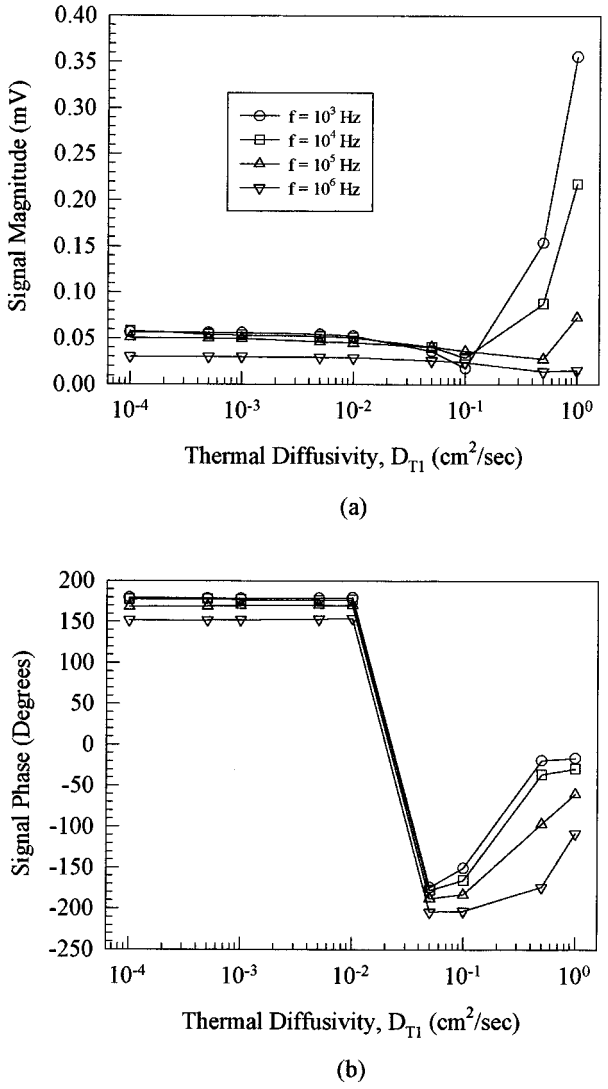

FIG. 12. PMTR signal vs thermal diffusivity D_{T_1} of the thin layer at various modulation frequencies; (a) Amplitude and (b) Phase. All other constants of the two layers are given in Tables I–III.

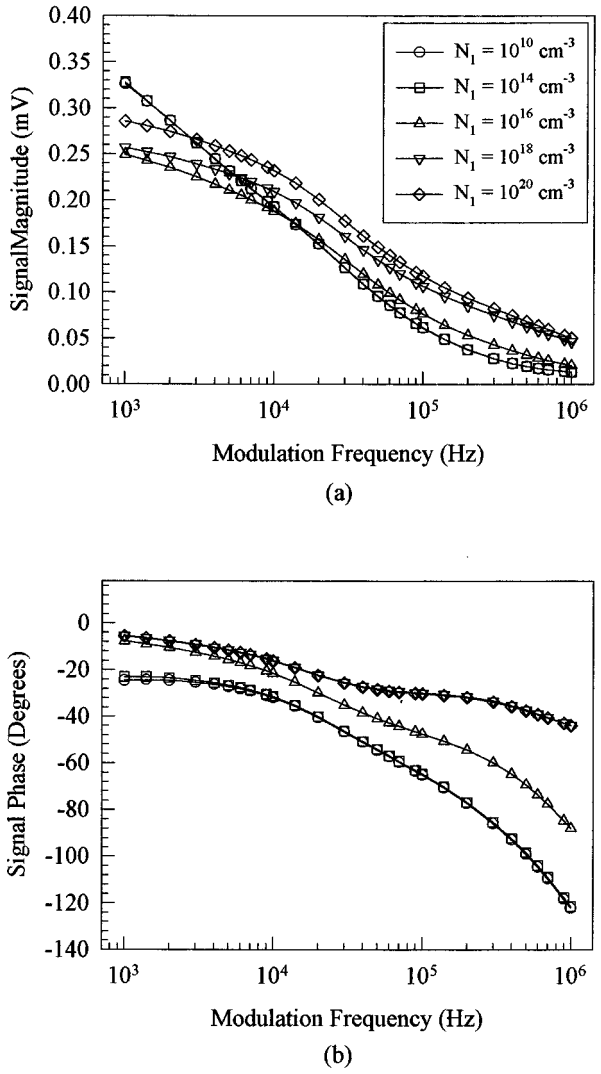

FIG. 13. PMTR signal vs modulation frequency for various concentrations N_1; (a) Amplitude and (b) Phase. All other constants of the two layers are given in Tables I–III.

launched thermal wave does not cross the boundary to the substrate, under the condition for the thermal diffusion length $\zeta_{T_1} \ll L_1$ (see Eq. (8)). Deviations occur for $D_{T_1} > 10^{-2}$ cm^2/s, when thermal-wave interferences between the front and back interfaces of the surface overlayer cause the curves to exhibit minima. This yields non-monotonic trends, also manifested in Fig. 1. A well-known characteristic of thermal-wave interferometry[24] is the shift of the amplitude minimum position to a higher diffusivity value as the modulation frequency increases, since these two parameters change the probe thermal diffusion length in the same direction. The position of the amplitude and phase minima in Fig. 12 can yield information on the value of the thermal diffusivity of the overlayer, if its thickness is known. The very large increases in the amplitude and phase shifts above the range of $D_{T_2} \approx 0.1$ cm^2/s are due to the eventual domination of the PMTR signal by the free plasma-wave of the substrate. Characteristic of this domination is the phase shift to negative values, as expected from the Drude term in Eq. (1).

D. Dependence on free-carrier concentration in the overlayer

In Secs. III A–III C the influence of various optical, electronic, and thermal properties of the thin surface layer on the PMTR signal was numerically calculated and physically discussed. The conclusions arrived at can provide only insights based on the artificial process of fixing all but one variable. This is not correct in practice,[19,20] but is very useful for giving indications of various trends. Following the same philosophy, in this last subsection, the dependence of the photothermal signal on the doping concentration of the thin surface layer is presented. Figure 13(a) shows the variation of the PMTR amplitude and phase as a function of modulation frequency for various doping densities of the thin surface layer from 1×10^{10} to 1×10^{20} cm^{-3}. In all cases the substrate doping density was 6×10^4 cm^{-3}. As was expected, both phase and amplitude decrease as a function of frequency. The co-incidence of curves □,○ with $N_1 < N_2$, indicates that it is impossible to photothermally measure con-

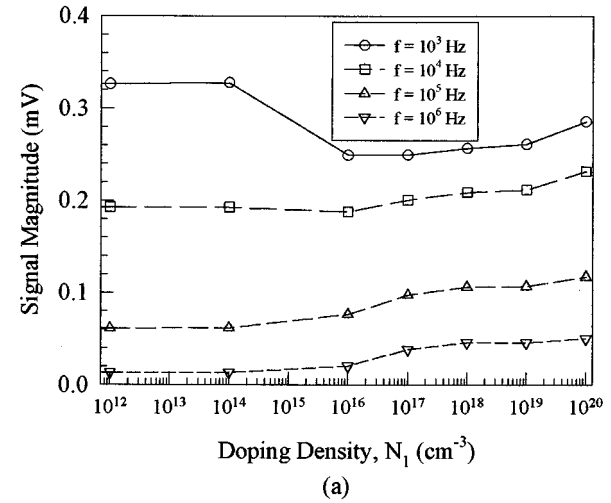

FIG. 14. PMTR signal vs concentration N_1 of the thin layer, for various modulation frequencies; (a) Amplitude and (b) Phase. All other constants of the two layers are given in Tables I–III.

centrations less than that of the dominating substrate at all experimentally attainable frequencies. Also difficult to measure experimentally are concentrations greater than 10^{18} cm^{-3} a screening phenomenon of the substrate by the free-carrier-saturated overlayer. Domination by the plasma-wave component is further indicated by the negative phase of the PMTR signal throughout much of the range of N_1 used in this simulation. The lack of saturation of the low-N_1 amplitude curves of (○,□) at low frequencies is an exception here, originating in thermal-wave domination of the PMTR signal in these regions, as expected from the very low plasma densities utilized in these simulations. The amplitude signal is weakly N_1-dependent for layer concentrations higher than that of the substrate, and so is the phase signal for concentrations between 10^{14} and 10^{17} cm^3. The trends in the PMTR signal with increasing doping density N_1 shown in Fig. 14 at various constant modulation frequencies clearly indicate that the overlayer generated plasma dominates the signal for $N_1 > 10^{16}$ cm^{-3} (both amplitude, Fig. 14(a), and phase, Fig. 14(b)). The non-monotonic behavior of the amplitude channel at low frequencies, also exhibited by the curves of Fig. 13(a) for $f < 10^4$ Hz, is generated by the gradual domination of the signal by the overlayer's plasma-wave component above $N_1 \approx 10^{14}$ cm^{-3} over the counteracting substrate's dominant thermal-wave component at lower values of N_1. Further increases in N_1 cause a net increase of the PMTR signal amplitude, as the overlayer screening of the thermal-wave in the substrate dominates. Higher modulation frequency signals are proportionally more affected by the substrate's plasma-wave component, to which the overlayer signal adds a term of the same sign, thus monotonically increasing the amplitude (curves: □,△,▽).

IV. CONCLUSIONS

The theory and simulations presented in this work show the features and potential of the photomodulated thermoreflectance technique as a complete non-contact and non-destructive quantitative characterization methodology of semiconducting processed wafers with an electronically active overlayer. This model is currently being utilized for quantitative analysis of annealing kinetics of defects in our laboratory. The present modeling on the variation of optical, thermal and electronic properties as functions of the annealing temperature may potentially yield depth-profilometric analysis on long and short-range disorder in processed semiconductors, if the relevant substrate properties are known or can be measured.

APPENDIX: MODULATED SURFACE FREE-CARRIER DENSITY AND TEMPERATURE IN HANKEL SPACE

This appendix calculates the Hankel transforms, $\Delta N_1(\lambda, z=0)$ and $\Delta T_1(\lambda, z=0)$ from the expressions in Eqs. (13) and (15). The analysis is divided into two parts, one for the derivation of each Hankel Transform.

A. Plasma density ΔN_1

First, the boundary condition at infinity given by Eq. (24), imposes $B_2(\lambda)=0$ in Eq. (14). From the boundary condition Eq. (21)

$$B_1(\lambda) = M_1(\lambda) A_1(\lambda) + M_2(\lambda), \tag{A1}$$

where

$$M_1(\lambda) = \frac{(s_1 + q_1(\lambda) D_{E_1})}{q_1(\lambda) D_{E_1} - s_1} \tag{A2}$$

and

$$M_2(\lambda) = \frac{(s_1 + \alpha_1 D_{E_1}) C_1(\lambda)}{q_1(\lambda) D_{E_1} - s_1} \tag{A3}$$

with

$$C_1(\lambda) = -\frac{\Phi \alpha_1}{D_{E_1}(\alpha_1^2 - q_1(\lambda)^2)} \Psi_p(\lambda). \tag{A4}$$

From Eq. (23):

$$A_2(\lambda) = M_3(\lambda) A_1(\lambda) + M_4(\lambda) \tag{A5}$$

and from Eq. (22)

$$A_1(\lambda) = \frac{M_4(\lambda)+C_2(\lambda)e^{-\alpha_2 z_1}-M_2(\lambda)e^{q_1 z_1}-C_1(\lambda)e^{-\alpha_1 z_1}}{e^{-q_1 z_1}+M_1(\lambda)e^{q_1 z_1}-M_3(\lambda)}, \tag{A6}$$

where $M_3(\lambda)$ and $M_4(\lambda)$ are given by the relations:

$$M_3(\lambda)=\frac{-q_1(\lambda)D_{E_1}e^{-q_1(\lambda)z_1}+D_{E_1}q_1(\lambda)e^{q_1(\lambda)z_1}M_1(\lambda)}{s_2-D_{E_2}q_2(\lambda)} \tag{A7}$$

and

$$M_4(\lambda)=\frac{E_1(\lambda)+E_2(\lambda)}{s_2-D_{E_2}q_2(\lambda)} \tag{A8}$$

with

$$E_1(\lambda)=D_{E_1}q_1(\lambda)e^{q_1 z_1}M_2(\lambda)-D_{E_1}\alpha_1 C_1(\lambda)e^{-\alpha_1 z_1} \tag{A9}$$

and

$$E_2(\lambda)=D_{E_2}\alpha_2 C_2(\lambda)e^{-\alpha_2 z_1}-s_2 C_2(\lambda)e^{-\alpha_2 z_1} \tag{A10}$$

$C_2(\lambda)$ is expressed by the following relation:

$$C_2(\lambda)=-\frac{\Phi\alpha_2\Psi_p(\lambda)}{D_{E_2}({\alpha_2}^2-q_2(\lambda)^2)}\,e^{-(\alpha_1-\alpha_2)z_1}. \tag{A11}$$

In the above equations $\Psi_p(\lambda)$, $p_1(\lambda)$, $p_2(\lambda)$, $q_1(\lambda)$, and $q_2(\lambda)$ were defined as the expressions:

$$\Psi_p(\lambda)=\frac{{a_p}^2}{4}\,e^{-\frac{\lambda^2 a_p^2}{8}}, \tag{A12}$$

$$p_j(\lambda)=\sqrt{{\zeta_{T_j}}^2+\lambda^2}; \quad j=1,2, \tag{A13}$$

$$q_j(\lambda)=\sqrt{{\zeta_{E_j}}^2+\lambda^2}; \quad j=1,2, \tag{A14}$$

where ζ_E and ζ_T were defined in Eqs. (7) and (8).

By introducing to Eq. (13) the constants $A_1(\lambda)$, $B_1(\lambda)$, and $C_1(\lambda)$ from Eqs. (A6), (A1) and (A4), respectively, and taking $z=0$ (surface), one obtains:

$$\Delta\hat{N}_1(\lambda,0)=A_1(\lambda)+B_1(\lambda)+C_1(\lambda). \tag{A15}$$

This Hankel function can be introduced into the integral of Eq. (29) in order to calculate the plasma contribution numerically.

B. Surface temperature, ΔT_1

Given our interest in the photothermal behavior at the surface, imposing $z=0$ on Eq. (15), yields

$$\Delta\hat{T}_1(\lambda,0)=Y_1(\lambda)A_1(\lambda)+Y_1(\lambda)B_1(\lambda)+H_1(\lambda)+L_1(\lambda)+Y_2(\lambda). \tag{A16}$$

All the foregoing terms can be evaluated from the boundary conditions, Eqs. (21)–(24). Thus,

$$Y_1(\lambda)=\frac{E_g}{\rho c\tau_1 D_{T_1}({p_1}^2(\lambda)-{q_1}^2(\lambda)} \tag{A17}$$

and

$$Y_2(\lambda)=\frac{\Phi\Psi_p(\lambda)\alpha_1}{\rho c D_{T_1}({p_1}^2(\lambda)-{\alpha_1}^2)}\left[\frac{E_g}{\tau_1 D_{E_1}({\alpha_1}^2-{q_1}^2(\lambda)}+(h\nu-E_g)\right] \tag{A18}$$

with

$$H_1(\lambda)=L_1(\lambda)+Y_5(\lambda), \tag{A19}$$

where $L_1(\lambda)$ is

$$L_1(\lambda)=Y_6(\lambda)H_2(\lambda)+Y_7(\lambda) \tag{A20}$$

and

$$H_2(\lambda)=\frac{Y_7(\lambda)[(e^{-p_1(\lambda)z_1}+e^{p_1(\lambda)z_1}]+Y_8(\lambda)}{1-Y_6(\lambda)[e^{-p_1(\lambda)z_1}+e^{p_1(\lambda)z_1}]} \tag{A21}$$

with

$$Y_8(\lambda)=G_1(\lambda)+G_2(\lambda). \tag{A22}$$

The functions-transforms G_1 and G_2 are defined as

$$G_1(\lambda)=Y_1(\lambda)A_1(\lambda)e^{-q_1(\lambda)z_1}+Y_1(\lambda)B_1(\lambda)e^{q_1(\lambda)z_1}-Y_4(\lambda)e^{-\alpha_2 z_1} \tag{A23}$$

and

$$G_2(\lambda)=Y_5(\lambda)e^{-p_1(\lambda)z_1}+Y_2(\lambda)e^{-\alpha_1 z_1}-Y_3(\lambda)A_2(\lambda). \tag{A24}$$

Also

$$Y_7(\lambda)=\frac{D_{T_1}Z(\lambda)+U(\lambda)+W(\lambda)}{V(\lambda)}, \tag{A25}$$

where

$$Z(\lambda)=G_3(\lambda)+G_4(\lambda). \tag{A26}$$

The function-transforms G_3 and G_4 are defined as

$$G_3(\lambda)=q_1(\lambda)Y_1(\lambda)A_1(\lambda)e^{-q_1(\lambda)z_1}-Y_1(\lambda)q_1(\lambda)B_1(\lambda)e^{q_1(\lambda)z_1} \tag{A27}$$

and

$$G_4(\lambda)=\alpha_1 Y_2(\lambda)e^{-\alpha_1 z_1}+Y_5(\lambda)p_1(\lambda)e^{-\alpha_1(\lambda)z_1}. \tag{A28}$$

Also in Eq. (A25):

$$V(\lambda)=D_{T_1}p_1(\lambda)[e^{p_1(\lambda)z_1}-e^{-p_1(\lambda)z_1}], \tag{A29}$$

$$W(\lambda)=-D_{T_2}[q_2(\lambda)Y_3(\lambda)A_2(\lambda)+\alpha_2 Y_4(\lambda)e^{-\alpha_2 z_1}], \tag{A30}$$

and

$$U(\lambda)=\frac{E_g s_2}{\rho c}\,[A_2(\lambda)+C_2(\lambda)e^{-\alpha_2 z_1}]. \tag{A31}$$

In Eqs. (A19) and (A20) the following definitions were also made:

$$Y_5(\lambda)=\frac{E_g s_1}{\rho c D_{T_1} p_1(\lambda)}\left[A_1(\lambda)+B_1(\lambda)+C_1(\lambda)\right]+G_5(\lambda) \tag{A32}$$

and

$$Y_6(\lambda)=-\frac{D_{T_2} p_2(\lambda)}{D_{T_1} p_1\left[e^{p_1(\lambda)z_1}-e^{-p_1(\lambda)z_1}\right]} \tag{A33}$$

with

$$G_5(\lambda)=\frac{Y_1(\lambda)q_1(\lambda)\left[B_1(\lambda)-A_1(\lambda)\right]-\alpha_1 Y_2(\lambda)}{p_1(\lambda)}. \tag{A34}$$

In Eqs. (A23) and (A24) the definitions Y_3 and Y_4 are

$$Y_3(\lambda)=\frac{E_g}{\rho c\,\tau_2 D_{T_2}\left[{p_2}^2(\lambda)-{q_2}^2(\lambda)\right]} \tag{A35}$$

and

$$Y_4(\lambda)=\frac{\Phi\Psi_p(\lambda)\alpha_2}{\rho c D_{T_2}\left(p_2(\lambda)^2-{\alpha_2}^2\right)}\left[\frac{E_g}{\tau_2 D_{E_2}\left({\alpha_2}^2-{q_2}^2(\lambda)\right)}+(h\nu-E_g)\right]e^{-(\alpha_1-\alpha_2)z_1}. \tag{A36}$$

[1] A. Rosencwaig, in *Photoacoustic and Thermal Wave Phenomena in Semiconductors*, edited by A. Mandelis (North Holland, New York, 1987), Chap. 5.

[2] A. Rosencwaig, in Progress in *Photothermal and Photoacoustic Science and Technology*, Vol. II, edited by A. Mandelis (Prentice Hall, Englewood Cliffs, New Jersey, 1993), Chap. 2.

[3] R. E. Wagner and A. Mandelis, Semicond. Sci. Technol. **11**, 289 (1996).

[4] J. Opsal, M. W. Taylor, W. L. Smith, and A. Rosencwaig, J. Appl. Phys. **61**, 240 (1987).

[5] J. Opsal and A. Rosencwaig, Appl. Phys. Lett. **47**, 498 (1985); J. Opsal, in *Review of Progress in Quantitative NDE*, edited by D. O. Thompson and D. E. Chimenti (Plenum, New York, 1987), p. 217; J. Opsal and A. Rosencwaig, *ibid*., p. 215; and J. Opsal, *ibid*., p. 1241.

[6] S. Wurm, P. Alpern, D. Savignac, and R. Kakoschke, Appl. Phys. A **47**, 147 (1988).

[7] N. M. Amer and W. B. Jackson, in *Semiconductors and Semimetals*, Vol. 21B, edited by J. I. Pankove (Academic, New York, 1984), pp. 83–112.

[8] J. Opsal, A. Rosencwaig, and D. L. Willenborg, Appl. Opt. **22**, 3169 (1983).

[9] V. A. Sablikov and V. B. Sandomirskii, Phys. Status Solidi B **120**, 471 (1983).

[10] M. Nestoros, B. C. Forget, C. Christofides, and A. Seas, Phys. Rev. B **51**, 14115 (1995).

[11] J. S. Blakemore, *Semiconductor Statistics* (Dover, New York, 1987), Chaps. 5 and 6.

[12] A. N. Vasiel'er and V. B. Sandomirskii, Sov. Phys. Semicond. **18**, 1095 (1984).

[13] B. C. Forget, Ph.D. thesis, Pierre and Marie Curie University, France, 1993.

[14] D. Fournier, A. C. Boccara, A. Skumanich, and N. M. Amer, J. Appl. Phys. **59**, 787 (1986).

[15] A. Mandelis, E. Siu, and S. Ho, Appl. Phys. A **33**, 153 (1984).

[16] A. Mandelis and A. Silva, Ferroelectrics **165**, 1 (1995).

[17] A. Seas and C. Christofides, Appl. Phys. A (in press).

[18] C. Christofides, *Photothermal Reflectance on Implanted and Annealed Semiconductors Wafers*, in *Semiconductor and Semimetals*, edited by C. Christofides and G. Guibaudo (Academic, New York) (to be published).

[19] R. F. Pierret, *Modular Series on Solid State Devices*, Vol. VI *Advanced Semiconductor Fundamentals*, edited by R. F. Pierret and G. W. Neudeck (Addison–Wesley, Reading 1987), pp. 188–192.

[20] S. M. Sze, *Physics of Semiconductors Devices* (Wiley, New York, 1965).

[21] A. Mandelis and B. S. H. Royce, J. Appl. Phys. **50**, 7138 (1979).

[22] A. Seas and C. Christofides, Appl. Phys. Lett. **66**, 3346 (1995).

[23] H. B. Bedd and E. W. Williams, in *Transport and Optical Phenomena*, edited by R. K. Willardson and A. C. Beer, *Semiconductors and Semimetals*, Vol. 8 (Academic, New York, 1972).

[24] C. A. Bennelt, Jr. and R. R. Patty, Appl. Opt. **21**, 49 (1982).